Editors' Suggestion | Featured in Physics

Mapping Thermal Expansion Coefficients in Freestanding 2D Materials at the Nanometer Scale

Xuan Hu,[1] Poya Yasaei,[2] Jacob Jokisaari,[1] Serdar Öğüt,[1] Amin Salehi-Khojin,[2] and Robert F. Klie[1]

[1]Department of Physics, University of Illinois at Chicago, Chicago, Illinois 60607, USA

[2]Department of Mechanical and Industrial Engineering, University of Illinois at Chicago, Chicago, Illinois 60607, USA

(Received 10 August 2017; revised manuscript received 15 December 2017; published 2 February 2018)

Two-dimensional materials, including graphene, transition metal dichalcogenides and their heterostructures, exhibit great potential for a variety of applications, such as transistors, spintronics, and photovoltaics. While the miniaturization offers remarkable improvements in electrical performance, heat dissipation and thermal mismatch can be a problem in designing electronic devices based on two-dimensional materials. Quantifying the thermal expansion coefficient of 2D materials requires temperature measurements at nanometer scale. Here, we introduce a novel nanometer-scale thermometry approach to measure temperature and quantify the thermal expansion coefficients in 2D materials based on scanning transmission electron microscopy combined with electron energy-loss spectroscopy to determine the energy shift of the plasmon resonance peak of 2D materials as a function of sample temperature. By combining these measurements with first-principles modeling, the thermal expansion coefficients (TECs) of single-layer and freestanding graphene and bulk, as well as monolayer MoS_2, $MoSe_2$, WS_2, or WSe_2, are directly determined and mapped.

DOI: 10.1103/PhysRevLett.120.055902

The combination of graphene, which has a zero band gap, with semiconducting two-dimensional (2D) transition metal dichalcogenides (TMDs) has the potential to revolutionize the field of high power and high frequency electronics, leading to novel nanometer-scale devices [1–9]. However, thermal management in such devices will be crucial because of the reduced dimensionality and high density of the devices in tightly packed structures [10–14]. It was previously suggested that the presence of grain boundaries and heterointerfaces has a significant impact on the overall thermal transport properties of devices based on 2D materials [15]. Therefore, a better understanding of the limits set by heat dissipation through grain boundaries and interfaces must be developed. One fundamental obstacle to overcome is the lack of spatial resolution in common temperature measurements.

To date, nanoscale thermometry is carried out either through scanning probe microscopy-based (SPM-based) techniques, like scanning thermal microscopy [16–20], or noncontact optical methods, such as Raman, fluorescence, and luminescence thermometry [21–23]. In SPM-based methods, the temperature is measured via a calibrated sensor fabricated on the tip of an AFM cantilever, such as a thermistor, where the electrical resistance is proportional to the temperature when the probe is in contact and in thermal equilibrium with the system. Although a spatial resolution of a few nanometers has been reported by performing the measurements in high vacuum [20], the resolution of these methods is limited by the size of the cantilever tip and the tip-surface contact characteristics. On the other hand, the noncontact optical techniques, such as Raman, fluorescence, and luminescence thermometry, utilize an indirect temperature-dependent phenomenon, then convert the measured signal into a temperature value. These techniques can provide an accurate temperature reading after a precise calibration, but the spatial resolution is limited by the optical diffraction limit. In both methods, particularly SPM, it is difficult to prepare freestanding specimens, and the measured material is often supported by a substrate. The effects of the substrate can be difficult to extract and will always impact the measurement.

In this Letter, we utilize noncontact thermometry beyond the optical diffraction limit using a combination of scanning transmission electron microscopy (STEM) and electron energy-loss spectroscopy (EELS) and first-principles modeling to map the local temperature and thermal expansion coefficient of 2D materials. More specifically, we develop an approach, based on the temperature-dependent plasmon energy shift, which is related to the thermal lattice expansion [24–27]. In 2D materials, such as graphene or TMDs, quantum confinement and surface plasmon effects dominate the energy shift of the plasmon peaks [28–30], providing a novel and universal approach for measuring the temperature and determining the thermal expansion coefficient of atomically thin structures, including metallic [31] and semiconductor materials.

Freestanding graphene, MoS_2, $MoSe_2$, WS_2, and WSe_2 were prepared for transmission electron microscopy analysis using liquid phase exfoliation and drop casting on a holey-carbon film coated Cu mesh. Low-loss EEL spectra

 © 2018 American Physical Society

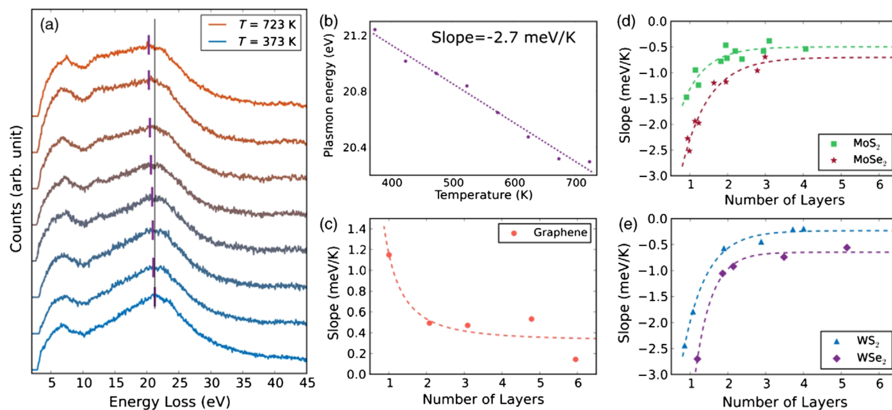

FIG. 1. (a) Low-loss EELS spectra from a monolayer of WSe_2 for temperatures between 373 K and 723 K. The purple lines indicate the plasmon peak centers for each temperature, determined by fitting two Lorentzian curves to the peak. The black line shows the plasmon peak center at a temperature of 373 K for comparison. (b) The plasmon energy for each spectrum from (a) as a function of the temperature. (c)–(e) The energy shifts (dE/dT) as a function of the number of layers of graphene, MoS_2, $MoSe_2$, WS_2, and WSe_2, respectively.

were collected for each material at eight different sample temperatures, between $T = 373$ K and 723 K in 50 K increments using a Gatan *in situ* heating holder. All spectra were calibrated using the zero-loss peak, and the low-loss intensity was normalized with respect to a 40–60 eV energy-loss window so that the normalization was not affected by the plasmon peak. The shift in plasmon energy as a function of the temperature was then measured for each material, thus providing a direct means of calibrating the temperature for each of the different materials and allowing the temperature to be mapped. The low-loss EEL spectra from a single monolayer of WSe_2 are shown in Fig. 1(a) for several temperatures. Since the plasmon peaks are relatively broad, we fit two Lorentzian functions to the individual plasmon peak to improve the accuracy of determining the plasmon peak energy shift (see Ref. [32] for more details). For WSe_2, the energy shift is $dE/dT = -2.7$ meV/K: A shift towards lower energy occurs as the temperature increases from 373 K to 723 K. This shift follows an approximately linear relationship between the plasmon energy and temperature [Fig. 1(b)]. Similar measurements are carried out for the materials.

The effects of layer thickness were also considered, ranging from monolayers to a few layers thick. The thickness, more specifically, the number of layers, was found to also influence the plasmon peak shift, and this effect needs to be accounted for in order to extract the temperature signal. To measure the thickness of the nanoflakes in units of number of layers, the ratio of the inelastically scattered over the transmitted electrons was determined using the low-loss EELS log-ratio method (see Ref. [32]). The rate of plasmon energy change as a function of temperature (dE/dT) for freestanding graphene and TMDs as a function of thickness is presented in Figs. 1(c)–1(e). Results indicate that graphene exhibits a positive energy shift compared to TMDs. Moreover, in TMDs containing Se, the plasmon energy shifts appear to be higher for all thicknesses compared to the corresponding TMD containing S. In all cases, the energy shift decreases as the number of layers increases, following an inverse square dependence. This thickness dependence seems to disappear for more than 3–4 layers. The inverse square dependence of the energy shift on thickness can be attributed to quantum confinement effects that become more pronounced as the thickness decreases [28,29]. Therefore, for materials that are 1–3 layers thick, we need to distinguish the energy shift of the plasmon peak due to changes in temperature from effects due to different sample thickness. This is achieved by measuring the temperature dependence of the plasmon energy shift separately for various 2D material thicknesses and applying the appropriate calibration measurement to map the temperature in an area of known thickness.

Using the thickness-dependent plasmon energy shifts, we determined the temperature distribution with nanometer-scale resolution in a $MoSe_2$ nanoflake, shown in the high-angle annular dark field (HAADF) image in Fig. 2(a), and the correlated plasmon-energy shift with the

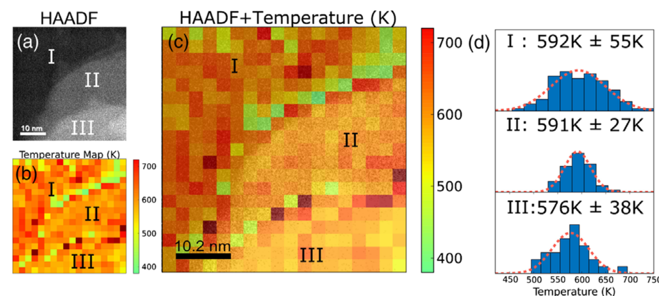

FIG. 2. (a) HAADF image of a $MoSe_2$ nanoflake. (b) Corresponding temperature map of $MoSe_2$ at a nominal sample temperature of 573 K. (c) The overlayed image of (a) and (b) showing three zones defined by the different thickness (I, II, III). (d) The temperature distribution for each area.

corresponding temperature map [shown in Fig. 2(b)]. This temperature map was created using the low-loss EELS signals acquired over the entire $MoSe_2$ flake, consisting of areas with different sample thickness labeled as I, II, and III that are 1, 2, and 3 layers thick, respectively. Using the calibrations shown in Figs. 1(d)–1(f) to account for the variation in thickness, a temperature map was produced for a $MoSe_2$ nanoflake at a setpoint temperature of 573 K. The overlay of the HAADF image and the temperature map [Fig. 2(c)] shows that, for the regions (I, II, III), we measured a temperature of approximately 586 K using the plasmon energy shift. Histograms showing the variation in temperature measured in each area are shown in Fig. 2(d). The temperature distributions are almost Gaussian, and by fitting a Gaussian function to the distribution, a mean temperature was calculated for each region. The error is expressed as the percentage difference from the holder-temperature setpoint (573 K). The measurements for areas (I, II, and III) are 592 K (3.3%), 591 K (3.1%), and 576 K (0.5%), respectively. One source of error in our measurements is related to finding the center of the plasmon peak, accounting for an uncertainty of ± 22 meV, which is relatively small compared to the peak shift of 270 meV per 100 K temperature difference in WSe_2, and it corresponds to a temperature uncertainty of 8 K. For mapping the edges of the 2D layers, there is an additional source of error due to changes in the plasmon peak shape at the layer edges [37]. This effect is visible in the temperature map, where the edges of the 2D layers appear cooler than the rest of the layer. However, the overall consistency and accuracy demonstrated in the measured temperature are well within the error of the sample holder-temperature setpoint, demonstrating that our technique is capable of mapping the temperature distribution at the nanoscale in 2D materials.

Thus far, our temperature measurements have been presented empirically, using a calibration curve of the plasmon energy shift as a function of temperature (dE/dT). Next, we show that the rate of this change is related to the lattice strain and the thermal expansion coefficient (TEC) of the material. This relationship is thickness dependent because of the quantum confinement effects, and it underpins our temperature measurements. Within the free electron model, the plasmon energy is expressed as

$$E(T) = \hbar\sqrt{\frac{n(T)e^2}{\varepsilon_0 m}}, \quad (1)$$

where m and e are the mass and charge of an electron. The temperature dependence of the electron density $n(T)$ is due to the temperature dependence of volume $V(T)$ of the valence electron cloud $n(T) = n_0/[V(T)]$, where n_0 is the number of valence electrons. Hence, dE/dT (measured experimentally) can be expressed in terms of the change in the plasmon energy as a function of the lattice parameters (determined computationally as discussed below) and the TEC. A more general derivation of dE/dT in terms of strain-induced plasmon shifts and TECs is provided in Ref. [32].

We employ this effect to determine the TECs for all five freestanding 2D materials studied here.

To determine the plasmon loss curves and the subsequent energy shifts as a function of the changes in the lattice parameters, we applied the random phase approximation (RPA) [38], a well-known approach for the calculation of frequency-dependent dielectric functions [$\varepsilon(\omega)$, which has been integrated into the Vienna *ab initio* simulation package (VASP) (see Methods Section in Ref. [32]) [39]]. In these calculations, the frequency-dependent dielectric function is determined by including local field effects, which allows the calculation of the low-loss EEL spectra [which is proportional to $\mathrm{Im}(-1/\varepsilon)$]. Low-loss EELS of graphene and TMDs were calculated for 10 different in-plane lattice constants, $a/a_0 = 0.97$–1.04, which correspond to the in-plane lattice parameters at different sample temperatures. For bulk materials, we also performed calculations with different out-of-plane (c) lattice parameters, and their corresponding plasmon energy shifts were determined by extrapolating the measured energy shifts shown in Figs. 1(c)–1(e) to the limit of infinitely large sample thickness.

An example of the calculated low-loss EEL spectra for graphene is shown in Fig. 3(a). We found a linear relationship between the plasmon energy and the lattice constant, shown in Fig. 3(b). With this computed relationship and the experimentally measured plasmon energy shift, the in-plane TECs were obtained for both thin films and bulk materials. The results are shown graphically in Fig. 3(c). Table I provides a complete list of TECs derived from our measurements and calculations for single-, double-, and trilayer, as well as bulk materials. The error bars in Table I

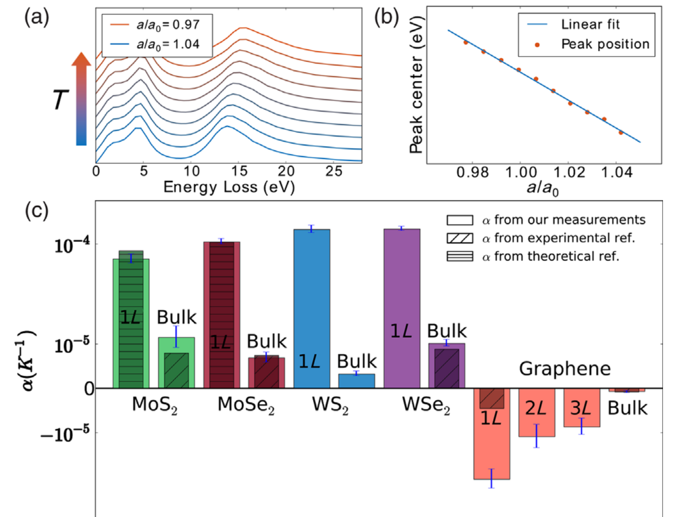

FIG. 3. (a) Calculated low-loss EEL spectra for single-layer graphene with different lattice constants. (b) The plasmon energy for each spectrum from (a) as a function of lattice constant a. (c) Measured in-plane TECs in thin films and bulk of graphene and TMDs, compared with reference data [40,43,47,48]. The error bars are shown in blue and are calculated using the experimental uncertainty in determining the plasmon energy shift.

TABLE I. Comparison of in-plane TECs (10^{-5} K^{-1}) obtained from our plasmon energy shift measurements and corresponding RPA calculations with reference (theoretical and experimental) data [40–48].

System	Monolayer	Bilayer	Trilayer	Bulk
MoS_2	6.49 ± 0.75 (8.24[a*])	3.60 ± 0.47	1.82 ± 0.25	1.15 ± 0.23 (0.66[b*], 0.49[c†] −0.79[d†])
$MoSe_2$	10.62 ± 0.64 (10.54[a*])	5.44 ± 0.35	3.46 ± 0.28	0.69 ± 0.10 (0.64[b*], 0.74[d†])
WS_2	15.21 ± 1.38	2.26 ± 0.20	1.31 ± 0.10	0.32 ± 0.04 (−0.15[b*], 0.64[f†])
WSe_2	15.42 ± 0.69	4.18 ± 0.25	2.74 ± 0.29	1.01 ± 0.06 (0.55[b*], 0.68[e†] −1.41[f†])
Graphene	-2.14 ± 0.37 (−0.31[g*], −0.45[h†])	-1.09 ± 0.25	-0.87 ± 0.17	-0.07 ± 0.01 (−0.04[g*], −0.08[i†])

[a]Ref. [40], [b]Ref. [41], [c]Ref. [42], [d]Ref. [43], [e]Ref. [44], [f]Ref. [45], [g]Ref. [46], [h]Ref. [47], [i]Ref. [48].
[*]Theoretical, [†]Experimental.

are computed using the scatter in the experimental data shown in Figs. 1(c)–1(e). Our predicted TEC values are compared with values available in the literature [40–48]. More details of the methods used to compute TECs are provided in Ref. [32].

As can be seen from Table I, our predictions for bulk materials are a close match with previously reported experimental data, especially for graphite, $MoSe_2$, and WSe_2. The consistency between the data reported here and the previously published data for bulk materials shows that the temperature dependence of the plasmon energy can be directly correlated with the thermal expansion. One important result of this study is that we experimentally measured the in-plane TECs for freestanding monolayer, bilayer, and trilayer TMDs. For monolayer TMDs, we found that the in-plane TECs agree well with the theoretical results [40], showing increased TEC values of even more than 1 order of magnitude compared to their bulk structures. This is consistent with our other observation that as the thickness increases from one layer to three layers (for graphene and TMDs), the TEC decreases.

While our reported TECs for TMDs agree very well with published values, the calculated TEC value for graphene differs substantially from the reference data while still exhibiting the correct overall trend. This likely arises from the very high thermal and electrical conductivity in graphene compared to the semiconducting TMDs. In particular, the temperature in nanoflakes of graphene is correlated to the mean free path of phonons, which is orders of magnitude larger in graphene compared to TMD materials. This means that the thermal transfer between the graphene and the carbon support is much more efficient than for the TMDs, and the temperature measurement is much less local. Another factor that may influence the difference between our measurements and the reference is substrate clamping. As the reference data are measured for graphene grown on a substrate, the TEC for freestanding graphene should be significantly larger.

To further demonstrate our ability to map the thermal expansion coefficient of freestanding 2D materials, we acquire maps of the plasmon peak in $MoSe_2$ nanoflakes at 473 K and 623 K (see Video 1 in Ref. [32]). The relative plasmon-peak shift as a function of position is measured and used to determine the TEC using the first-principles modeling results described above. Figure 4(a) shows a freestanding $MoSe_2$ flake at 623 K, as well as the measured

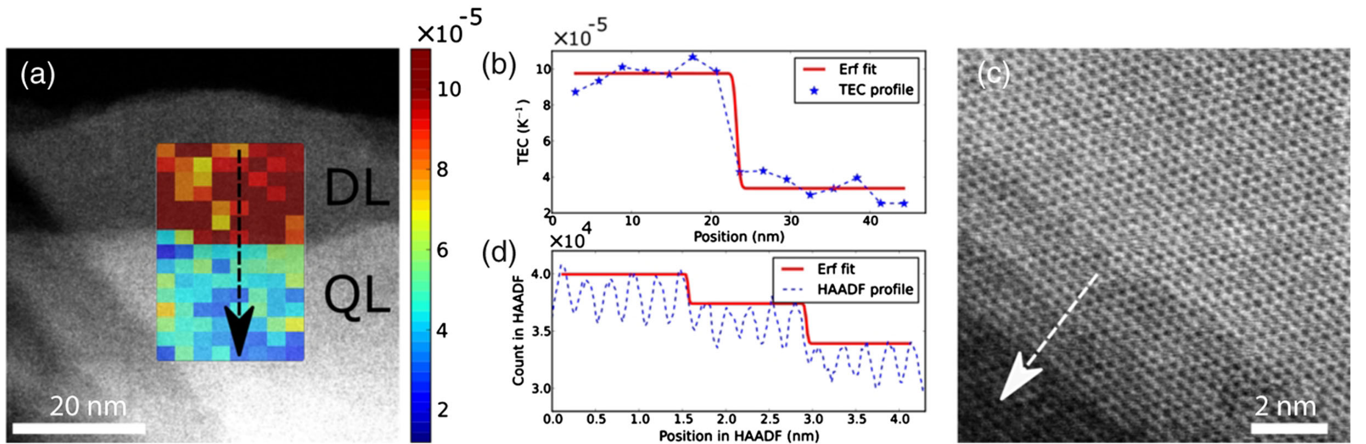

FIG. 4. (a) HAADF image of $MoSe_2$ at 623 K and the spatially resolved map of the local thermal expansion coefficient in the edge between double-layer (DL) and four-layer (QL) areas. (b) Line profile of thermal expansion coefficient of the interface indicated by the black line in (a). (c) Representative atomic-resolution HAADF image of MoS_2 taken at 573 K. (d) Line profile of image contrast across several layers of MoS_2 at 573 K.

thermal expansion coefficient. The region of the $MoSe_2$ shown in Fig. 4(a) consists of two different layers, each exhibiting a different thermal expansion coefficient ranging between 0.25 and $1.06 \times 10^{-4}\ K^{-1}$. It is interesting to note here that the double-layer area appears to exhibit the highest thermal expansion coefficient and a sharp decrease at the edges of the layer. Figure 4(b) shows a line profile of the edge between the double and four-layer regions in $MoSe_2$. It appears that the spatial resolution of the thermal expansion coefficient map is 2.95 nm and is mostly limited by the pixel size of the spectrum image. To get a subpixel estimate of the position of the edge, a complementary error function is fitted through the experimental data, revealing that the measured width of the interface can be as small as 2.1 nm, if smaller pixel sizes are used for mapping the plasmon peak shift.

Figure 4(c) shows an atomic-resolution HAADF image of a freestanding MoS_2 flake at elevated temperature (573 K) consisting of four distinctive layers, and it demonstrates that the spatial resolution for imaging (even at elevated temperatures) is better than 1 Å [Fig. 4(d)]. However, the spatial resolution limit for our TEC measurements at interfaces and defects using STEM-EELS is lower than this value, as the temperature measurements fundamentally depend on the mean free path of phonons and electrons [31]. More specifically, the localization of the EELS signal for a plasmon peak at 20 eV can be determined using the equation introduced by Egerton [49]:

$$d_{50} \approx \sqrt{\left(\frac{\lambda}{2\theta_E^{3/4}}\right)^2 + \left(\frac{0.6\lambda}{\beta}\right)^2} \approx 1.9\ \text{nm}, \qquad (2)$$

where $\lambda = 2.51$ pm is the electron wavelength at 200 kV, $\theta_E = 0.06$ mrad is the characteristic scattering angle, and $\beta = 60$ mrad is the EELS collection angle. On the practical side, the current measurement resolution is also limited by spatial drift and the sensitivity of the 2D materials to extended electron beam exposure. Nevertheless, the spatial resolution shown in Fig. 4(b) is very close to the predicted theoretical limit at the given plasmon peak energy and orders of magnitude better compared to the spatial resolution of 100 nm for optical techniques. Such a high resolution for TEC measurements is crucial for examining thermal expansion mismatch and strain in the latest sub-10-nm transistors [50], where direct measurements are only possible using our STEM-EELS method. Further improvements to the temperature resolution and accuracy can be achieved by increasing the energy resolution of the low-loss EEL spectra using, for example, a monochromated STEM instrument [43]. More importantly, the measurement rate of our technique is very high, providing the capability of capturing dynamic temperature changes. The exposure time for low-loss EELS can be as low as 10^{-3} s, with a sufficient signal-to-noise ratio for most thin materials. This provides a great potential for *in situ* thermal experiments involving dynamic processes. Finally, it should be noted that a potential issue arises from electron-beam-induced sample heating effects. However, using a thermal conductivity κ of around 1 $Wm^{-1} K^{-1}$ for WSe_2 [51], we found a beam-induced temperature rise of only $\Delta T \approx 0.95$ mK for the electron probe conditions used. This value is significantly smaller than the temperature resolution of our EELS-based measurement and may safely be neglected. Details of the beam heating contributions are discussed in Ref. [32].

In summary, we have presented a novel approach to nanoscale mapping of TECs in freestanding 2D materials using high-resolution STEM imaging coupled with EEL spectroscopy. The measurement utilizes the shift in the plasmon peak of the 2D material, which is related to the thermal expansion of the 2D lattice. The measured plasmon energy shift exhibits a dependence on the number of 2D layers, which is attributed to quantum confinement effects in 2D materials. Accounting for the sample thickness of the 2D material, in units of number of atomic layers, we showed that it is possible to map the local temperature with nanometer resolution. Theoretical calculations using DFT and RPA were also developed to compare the thermal expansion coefficients of 2D and bulk materials, and the results are found to be in quite good agreement with existing reference data. By measurement of the TEC near surfaces, grain boundaries or heterointerfaces, we can predict and control the mismatch and thermal strain resulting from various device operations, avoiding strain-induced (thermomechanical) fracture or changes in the electronic properties. This is particularly important for 2D materials, where temperature changes can cause strains on both sides of the interface because of the thickness dependence of the TEC. Future studies examining temperature variations across heterointerface or grain boundaries, or other low-dimensional structures such as nanowires, in-plane heterostructures, and hybrid nanostructures, will be essential to further elucidate our understanding of the thermal transport properties in nanoscale devices.

X. H., A. S. K., and R. F. K. were supported by the National Science Foundation EFRI 2-DARE Grant No. EFMA-1542864. Dr. D. P. Bailey of the University of Illinois College of Engineering assisted in the copy editing of the manuscript. The acquisition of the JEOL JEM-ARM200CF at the University of Illinois at Chicago is supported by an MRI-R^2 grant from the National Science Foundation (Grant No. DMR-0959470). This work made use of instruments in the Electron Microscopy Service and the High Performance Computing Clusters at Research Resources Center, UIC. This work used resources of the National Energy Research Scientific Computing Center, a DOE Office of Science User Facility supported by the Office of Science of the U.S. Department of Energy under Contract No. DE-AC02-05CH11231.

[1] A. K. Geim and K. S. Novoselov, Nat. Mater. **6**, 183 (2007).
[2] K. I. Bolotin, K. J. Sikes, Z. Jiang, M. Klima, G. Fudenberg, J. Hone, P. Kim, and H. L. Stormer, Solid State Commun. **146**, 351 (2008).
[3] A. A. Balandin, S. Ghosh, W. Bao, I. Calizo, D. Teweldebrhan, F. Miao, and C. N. Lau, Nano Lett. **8**, 902 (2008).
[4] F. Schwierz, Nat. Nanotechnol. **5**, 487 (2010).
[5] Z. Yan, G. Liu, J. M. Khan, and A. A. Balandin, Nat. Commun. **3**, 827 (2012).
[6] W. Han, R. K. Kawakami, M. Gmitra, and J. Fabian, Nat. Nanotechnol. **9**, 794 (2014).
[7] B. Radisavljevic, A. Radenovic, J. Brivio, V. Giacometti, and A. Kis, Nat. Nanotechnol. **6**, 147 (2011).
[8] W. J. Yu, Q. A. Vu, H. Oh, H. G. Nam, H. Zhou, S. Cha, J.-Y. Kim, A. Carvalho, M. Jeong, H. Choi, A. H. Castro Neto, Y. H. Lee, and X. Duan, Nat. Commun. **7**, 13278 (2016).
[9] F. H. L. Koppens, T. Mueller, P. Avouris, A. C. Ferrari, M. S. Vitiello, and M. Polini, Nat. Nanotechnol. **9**, 780 (2014).
[10] Y. Li, W. Zhou, H. Wang, L. Xie, Y. Liang, F. Wei, J.-C. Idrobo, S. J. Pennycook, and H. Dai, Nat. Nanotechnol. **7**, 394 (2012).
[11] R. Murali, K. Brenner, Y. Yang, T. Beck, and J. D. Meindl, IEEE Electron Device Lett. **30**, 611 (2009).
[12] L. Britnell, R. V. Gorbachev, R. Jalil, B. D. Belle, F. Schedin, A. Mishchenko, T. Georgiou, M. I. Katsnelson, L. Eaves, S. V. Morozov, N. M. R. Peres, J. Leist, A. K. Geim, K. S. Novoselov, and L. A. Ponomarenko, Science **335**, 947 (2012).
[13] Q. H. Wang, K. Kalantar-Zadeh, A. Kis, J. N. Coleman, and M. S. Strano, Nat. Nanotechnol. **7**, 699 (2012).
[14] D. Lembke, S. Bertolazzi, and A. Kis, Acc. Chem. Res. **48**, 100 (2015).
[15] P. Yasaei, A. Fathizadeh, R. Hantehzadeh, A. K. Majee, A. El-Ghandour, D. Estrada, C. Foster, Z. Aksamija, F. Khalili-Araghi, and A. Salehi-Khojin, Nano Lett. **15**, 4532 (2015).
[16] A. Majumdar, J. Lai, M. Chandrachood, O. Nakabeppu, Y. Wu, and Z. Shi, Rev. Sci. Instrum. **66**, 3584 (1995).
[17] Y. De Wilde, F. Formanek, R. Carminati, B. Gralak, P.-A. Lemoine, K. Joulain, J.-P. Mulet, Y. Chen, and J.-J. Greffet, Nature (London) **444**, 740 (2006).
[18] A. Soudi, R. D. Dawson, and Y. Gu, ACS Nano **5**, 255 (2011).
[19] F. Menges, H. Riel, A. Stemmer, and B. Gotsmann, Nano Lett. **12**, 596 (2012).
[20] F. Menges, P. Mensch, H. Schmid, H. Riel, A. Stemmer, and B. Gotsmann, Nat. Commun. **7**, 10874 (2016).
[21] I. Calizo, A. A. Balandin, W. Bao, F. Miao, and C. N. Lau, Nano Lett. **7**, 2645 (2007).
[22] K. Okabe, N. Inada, C. Gota, Y. Harada, T. Funatsu, and S. Uchiyama, Nat. Commun. **3**, 705 (2012).
[23] C. D. S. Brites, P. P. Lima, N. J. O. Silva, A. Millan, V. S. Amaral, F. Palacio, and L. D. Carlos, Nanoscale **4**, 4799 (2012).
[24] H. Watanabe, J. Phys. Soc. Jpn. **11**, 112 (1956).
[25] G. Meyer, Z. Phys. **148**, 61 (1957).
[26] H. Abe, M. Terauchi, and M. Tanaka, J. Electron Microsc. **44**, 45 (1995).
[27] H. Abe, M. Terauchi, R. Kuzuo, and M. Tanaka, J. Electron Microsc. **41**, 465 (1992).
[28] M. Mitome, Y. Yamazaki, H. Takagi, and T. Nakagiri, J. Appl. Phys. **72**, 812 (1992).
[29] Y. Wang, J. Kim, G. Kim, and K. Kim, Appl. Phys. Lett. **88**, 143106 (2006).
[30] T. Eberlein, U. Bangert, R. R. Nair, R. Jones, M. Gass, A. L. Bleloch, K. S. Novoselov, A. Geim, and P. R. Briddon, Phys. Rev. B **77**, 233406 (2008).
[31] M. Mecklenburg, W. A. Hubbard, E. R. White, R. Dhall, S. B. Cronin, S. Aloni, and B. C. Regan, Science **347**, 629 (2015).
[32] See Supplemental Material http://link.aps.org/supplemental/10.1103/PhysRevLett.120.055902 for a description of experimental methods and first-principles modeling, as well as additional data of the EELS plasmon peak shifts as a function of temperature, which includes Refs. [33–36].
[33] M. Asadi, K. Kim, C. Liu, A. V. Addepalli, P. Abbasi, P. Yasaei, P. Phillips, A. Behranginia, J. M. Cerrato, R. Haasch, P. Zapol, B. Kumar, R. F. Klie, J. Abiade, L. A. Curtiss, and A. Salehi-Khojin, Science **353**, 467 (2016).
[34] Y. Hernandez, V. Nicolosi, M. Lotya, F. M. Blighe, Z. Sun, S. De, I. T. McGovern, B. Holland, M. Byrne, Y. K. Gun'ko, J. J. Boland, P. Niraj, G. Duesberg, S. Krishnamurthy, R. Goodhue, J. Hutchison, V. Scardaci, A. C. Ferrari, and J. N. Coleman, Nat. Nanotechnol. **3**, 563 (2008).
[35] A. Politano and G. Chiarello, Nanoscale **6**, 10927 (2014).
[36] E. R. White, M. Mecklenburg, B. Shevitski, S. B. Singer, and B. C. Regan, Langmuir **28**, 3695 (2012).
[37] W. Zhou, S. J. Pennycook, and J.-C. Idrobo, Ultramicroscopy **119**, 51 (2012).
[38] S. Louie, J. Chelikowsky, and M. Cohen, Phys. Rev. Lett. **34**, 155 (1975).
[39] G. Kresse and J. Hafner, Phys. Rev. B **47**, 558 (1993).
[40] D. J. Late, S. N. Shirodkar, U. V. Waghmare, V. P. Dravid, and C. N. R. Rao, ChemPhysChem **15**, 1592 (2014).
[41] Y. Ding and B. Xiao, RSC Adv. **5**, 18391 (2015).
[42] R. Murray and B. Evans, J. Appl. Crystallogr. **12**, 312 (1979).
[43] S. Elmahalawy and B. Evans, J. Appl. Crystallogr. **9**, 403 (1976).
[44] L. H. Brixner, J. Electrochem. Soc. **110**, 289 (1963).
[45] A. Matthaus, A. Ennaoui, S. Fiechter, S. Tiefenbacher, T. Kiesewetter, K. Diesner, I. Sieber, W. Jaegermann, T. Tsirlina, and R. Tenne, J. Electrochem. Soc. **144**, 1013 (1997).
[46] N. Mounet and N. Marzari, Phys. Rev. B **71**, 205214 (2005).
[47] W. Pan, J. Xiao, J. Zhu, C. Yu, G. Zhang, Z. Ni, K. Watanabe, T. Taniguchi, Y. Shi, and X. Wang, Sci. Rep. **2**, 893 (2012).
[48] A. Bailey and B. Yates, J. Appl. Phys. **41**, 5088 (1970).
[49] R. F. Egerton, *Electron Energy Loss Spectroscopy in the Electron Microscope* (Plenum Press, New York, 1986).
[50] A. D. Franklin, M. Luisier, S.-J. Han, G. Tulevski, C. M. Breslin, L. Gignac, M. S. Lundstrom, and W. Haensch, Nano Lett. **12**, 758 (2012).
[51] A. Mavrokefalos, N. T. Nguyen, M. T. Pettes, D. C. Johnson, and L. Shi, Appl. Phys. Lett. **91**, 171912 (2007).